Physicochem. Probl. Miner. Process., 62(5), 2026, 242846

http://www.journalssystem.com/ppmp

Physicochemical Problems of Mineral Processing

ISSN 1643-1049
© Wroclaw University of Science and Technology

Reduced-order polynomial representation of dem-derived impact and shear energy profiles on mill lifters

Hüseyin Efe Selvi [1], Tahir Abbas Jauhar [1], Yusuf Enes Pural [2]

[1] University of Newcastle, Centre for Bulk Solids and Particulate Technologies, Newcastle, Australia

[2] Istanbul Technical University, Mineral Processing Engineering Department, Istanbul, Turkey

Corresponding author: HuseyinEfe.Selvi@newcastle.edu.au (Hüseyin Efe Selvi)

Abstract: Comminution processes in the mineral industry are notoriously energy-intensive, with tumbling mills relying heavily on internal lifters to dictate charge motion, optimize particle breakage, and facilitate energy transfer. As these lifters inevitably degrade during operation, mill performance, throughput, and energy efficiency decline significantly. Therefore, the precise characterization and prediction of mill lifter wear is critical for optimizing grinding efficiency and improving predictive maintenance strategies in mineral processing. In this numerical study, the Discrete Element Method (DEM) framework was employed to simulate the wear mechanisms governing lifter degradation in a tumbling mill. Using impact and shear energy spectra derived from DEM simulations, an energy-equivalent Archard formulation was applied to the cumulative normal and tangential contact-energy fields from one DEM operating condition. The simulated mill, 4000 mm in diameter and 6000 mm in length, operated at 71.4% of critical speed with 24 lifters and a nominal charge filling of 30%. The lifters have geometry as 150 mm height and 60° face angle. To further investigate the spatial wear on the various faces of the lifter, the energy distributions from 24 lifters were mapped into five physically meaningful regions: Leading Face Plate, Leading Face, Top, Trailing Face and Trailing Face Plate. Median impact and shear energies were extracted and reconstructed using cubic polynomials, producing within-case coefficients of determination of $R^2 = 0.99$ and $R^2 = 0.94$ respectively. The ordinary least squares method was used to fit cubic polynomials. Future work will focus on investigating the relationship between the obtained polynomial fits and mill operating conditions as well as liner geometry, aiming to enhance the predictive capability of the model under varying scenarios. The formulation should therefore be regarded as a case-specific reduced-order representation; independent operating-condition and fixed-geometry validation remain necessary.

Keywords: tumbling mill, DEM modelling, Archard's wear law, lifter geometry, energy analysis

1. Introduction

Comminution is one of the most energy-intensive operations in the mining and mineral-processing industries, with tumbling mills accounting for a substantial proportion of the electrical energy consumed during mineral production (Fuerstenau and Abouzeid, 2002; Tromans, 2008; Jeswiet and Szekeres, 2016). Despite this high energy demand, only a small fraction of the mechanical energy supplied to a mill contributes directly to useful particle breakage, while the remaining energy is dissipated through particle motion, friction, deformation, and heat generation (Cleary, 2001). Improving the transfer and utilisation of energy within grinding mills is therefore important for reducing operating costs and the environmental footprint associated with mineral processing (Holmberg et al., 2017).

Mill liners and lifters strongly influence this energy-transfer process by controlling the motion, elevation and release of the grinding charge. Variations in lifter height, face angle, spacing and profile modify the shoulder and toe positions of the charge, the trajectories of grinding media, and the balance between cascading and cataracting motion (Powell, 1991; Hlungwani et al., 2003; Powell et al., 2006; Bian et al., 2017). These changes affect both comminution performance and the spatial distribution of loading on the liner surface. Lifter degradation is generally associated with a combination of high-

DOI: 10.37190/ppmp/242846

energy normal interactions and sustained tangential or abrasive contacts (Akhondizadeh et al., 2016; Soleymani et al., 2022). As the lifter profile changes during operation, charge motion, power draw, throughput, and product-size distribution may also change, making the characterisation of lifter wear important for mill design and maintenance planning (Yahyaei et al., 2009; Powell et al., 2011; Cleary and Owen, 2018).

Industrial liner wear has traditionally been evaluated using plant inspections, manual profile measurements, and three-dimensional laser scanning during scheduled shutdowns. These methods provide valuable information about the magnitude and spatial non-uniformity of wear after a period of operation (Banisi and Hadizadeh, 2007; Yahyaei et al., 2009). However, they are primarily retrospective and depend on access to an operating mill. Their ability to assess an untested lifter geometry or operating condition is therefore limited unless additional plant trials or detailed empirical calibration are undertaken.

The Discrete Element Method (DEM) provides an alternative means of investigating particle-scale behaviour inside tumbling mills by resolving particle trajectories, collisions and contact forces. DEM has been applied to predict charge motion, power draw, liner loading, and collision-energy distributions under different mill conditions (Mishra and Rajamani, 1992, 1994; Cleary, 2001; Bian et al., 2017). The method has also been combined with phenomenological wear formulations, including adaptations of Archard's wear law, to estimate spatial material loss from DEM-derived contact quantities (Kalala et al., 2005; Franke et al., 2015; Boemer and Ponthot, 2017; Xu et al., 2018). Nevertheless, high-resolution DEM wear calculations remain computationally demanding and generate large, irregular, and strongly skewed datasets. The resulting energy fields may contain many low-intensity interactions together with a relatively small number of highly energetic local contacts, making direct interpretation and comparison difficult.

Most DEM-based liner-wear studies consequently rely on cumulative wear indicators, averaged collision quantities, or contour maps of selected liner regions. Although these representations are useful, they do not always provide a compact analytical description of how normal and tangential contact energies vary continuously across the different faces of an individual lifter (Pural et al., 2024; Jauhar et al., 2026a). A reduced-order representation of these spatial distributions could assist interpretation of the DEM output, simplify comparison between energy mechanisms, and provide an intermediate description between mesh-level simulation data and future surrogate modelling. However, such a representation must preserve the principal asymmetry of the energy profile without implying predictive capability beyond the conditions from which it was obtained.

The present study therefore develops a region-based procedure for representing DEM-derived impact-associated normal energy and shear-associated tangential energy across the surface of a wedge-bar mill lifter. The lifter profile is divided into five physically defined regions: the leading face plate, leading face, top, trailing face, and trailing face plate. Representative regional energy values are calculated from the DEM surface data and expressed along a normalised lifter-profile coordinate. Low-order polynomial functions are then assessed as compact mathematical descriptions of the resulting regional energy profiles. The fitting procedure is intended to condense the spatial DEM output while retaining the principal differences between normal- and shear-energy distributions.

The specific objectives of this study are to:

1. Quantify the spatial distributions of normal and shear contact energy obtained from the DEM simulation;
2. Aggregate these distributions across five defined regions of the lifter surface;
3. Construct and evaluate a compact polynomial representation of the regional energy profiles; and
4. Examine the applicability and limitations of the proposed representation as a reduced-order description of DEM-derived liner-loading data.

The analysis is based on one DEM operating condition. Accordingly, the fitted polynomial coefficients are treated as case-specific mathematical descriptors of the investigated energy profiles rather than as universal physical constants. The present study does not establish causal relationships between individual polynomial coefficients and mill speed, filling level, load intensity or lifter geometry. Determining such relationships would require a systematically varied, multi-condition dataset and independent validation. The contribution of the present work is therefore limited to

demonstrating and critically evaluating the proposed data-reduction procedure for the simulated condition.

2. Methodology

2.1. DEM setup

Particle–lifter interactions were simulated using a Discrete Element Method (DEM) framework (Mishra & Rajamani, 1994; Cleary, 2001). The simulated mill had an internal diameter of 4.0 m and an axial length of 6.0 m. No conical section was included in the geometry: both the cone angle and cone length were set to zero. The mill was therefore represented as a cylindrical chamber bounded by two flat axial end walls. No discharge opening, slurry flow, or continuous material feed was activated, and the model consequently represented a closed batch system.

The mill was equipped with 24 identical lifters distributed uniformly around the internal circumference, corresponding to an angular spacing of 15°. Each lifter extended continuously along the full 6.0 m axial length of the mill. The lifters had a height of 0.150 m and a circumferential width of 0.150 m. The left- and right-face-angle inputs in the model were 60° and 90°, respectively. A second or alternating lifter geometry was not activated. The mill shell and lifters were assigned a steel density of 7850 kg/m^3.

A signed rotational speed of −15 *rpm* was prescribed in the model. The negative sign specifies the selected rotational direction according to the software coordinate convention, while the rotational-speed magnitude was 15 *rpm*. This corresponded to 71.4% of the critical speed reported for the investigated case. The simulation was run for five complete mill revolutions, equivalent to 20 s of simulated operating time.

The charge filling input was set to 30 vol%, defined as the nominal volume occupied by the generated particulate charge relative to the internal volume of the mill. This was the only volumetric filling input identified in the project setup. Therefore, the previously reported separate values of "filling degree 30%" and "load level 30%" are not treated as independent operating variables (Powell et al., 2006).

The physical-wear and physical-lifter-wear options were disabled during the DEM calculation. Consequently, the shell and lifter geometry remained fixed throughout the five-revolution simulation. The mill-wear, mill-impact, and energy-spectrum analysis options were enabled to accumulate contact-related quantities on the fixed surface mesh. The calculated wear field therefore represents an energy-based diagnostic applied to the original geometry rather than an iterative simulation in which the liner geometry was progressively deformed or remeshed (Table 1).

2.1.1. Particulate charge properties

The simulated charge consisted of a single population of monosized spherical particles. Therefore, no particle-size distribution was implemented in the present DEM model. All particles had the same nominal diameter; however, the numerical value of this diameter was not retained in the available simulation records and could not be recovered during preparation of the revised manuscript. Based on the reported particle count, total charge mass, and corrected density, an equivalent particle diameter of approximately 48.46 mm was estimated, assuming identical solid spheres. The absence of the nominal particle diameter is acknowledged because particle size influences particle population, collision frequency, contact duration, energy dissipation, and the appropriate numerical time step.

The particles were assigned a density of 7850 kg/m^3, a shear modulus of 10 MPa, and a Poisson's ratio of 0.30. The charge was represented using spherical particles and occupied 30 vol% of the internal mill volume. The available project summary indicated approximately 227,812 particles with a total charge mass of approximately 106,535 kg; At 30% charge filling, the particle density of 7850 kg/m^3 corresponds to an estimated solids packing fraction of approximately 0.60. These values are reported as model summary quantities.

Only one particulate population was identified in the available simulation setup. Consequently, the revised manuscript does not distinguish between separate ore and grinding-ball size distributions. The terms particulate charge, particles, and media are used consistently to describe the simulated spherical charge. This simplification should be considered when interpreting the resulting collision-energy distributions, since an industrial tumbling mill commonly contains a wider range of particle and grinding-media sizes (Table 2).

Table 1. DEM parameters input

Category	Parameter	Value or model setting
Software	Model-preparation environment	EZMill v1.0
Mill configuration	Mill type	Batch ball-mill configuration
Mill geometry	Internal diameter	4.000 m
	Axial length	6.000 m
	Cone angle	0°
	Cone-section length	0.000 m
	Axial end geometry	Two flat end walls
	Discharge opening	Not activated
	Slurry phase	Not activated
Operation	Signed rotational speed	−15 *rpm*
	Rotational-speed magnitude	15 *rpm*
	Critical-speed ratio	71.4%
	Simulation duration	5 revolutions
	Equivalent simulated time	20 s
	Charge filling	30 vol% of internal mill volume
Lifter configuration	Number of lifters	24
	Circumferential spacing	15°
	Axial extent	Full 6.0 m mill length
	Lifter height	0.150 m
	Lifter width	0.150 m
	Left-face angle	60°
	Right-face angle	90°
	Alternating/second lifter	Not activated
Boundary material	Shell and lifter density	7850 kg m^{-3}
Wear treatment	Physical geometry deformation	Disabled
	Physical lifter-wear option	Disabled
	Energy-spectrum analysis	Enabled
	Mill-impact analysis	Enabled
	Mill-wear calculation	Enabled
	Energy-spectrum bin width	0.01 J

Table 2. Properties of the particulate charge used in the DEM model

Parameter	Value or model description
Number of particulate populations	One
Particle representation	Spherical
Particle-size condition	Monosized/monodisperse
Particle-size distribution	Not applicable
Nominal particle diameter	Not available in the retained simulation records
Particle density	7850 kg/m^3
Shear modulus	10 MPa
Poisson's ratio	0.30
Charge filling	30 vol% of internal mill volume
Approximate particle count	227,812
Approximate total charge mass	106,535 kg
Particle breakage	Not represented in the reported energy-profile analysis
Slurry or fluid phase	Not included
Separate ore and ball populations	Not activated in the available setup

2.1.2. Contact model and interaction parameters

Interactions between the particulate media and between the media and steel mill boundaries were represented using the Hertz–Mindlin contact model. In this formulation, the normal contact response is based on nonlinear Hertzian elasticity combined with velocity-dependent damping, while the tangential response is represented using a Mindlin-type incremental tangential-force formulation limited by the Coulomb friction criterion.

The coefficient of restitution controls the damping of the normal relative motion during collision. A particle–particle restitution coefficient of 0.30 and a particle–steel restitution coefficient of 0.50 were used. These coefficients influence collision damping and resulting energy dissipation; their sensitivity was not independently evaluated in this study (Wang et al., 2025). Static-friction coefficients of 0.50 were assigned to both particle–particle and particle–steel interactions. Rolling resistance was included using the software's built-in rolling-friction treatment, with coefficients of 0.10 for both interaction types (Table 3). The adopted particle shear modulus of 10 MPa represents a reduced-stiffness approximation that may affect contact overlap and energy dissipation; its sensitivity remains to be assessed (Lommen et al., 2014; Ghasemi et al., 2020). Recent research by Hu et al. (2027) demonstrated the integration of industrial liner-wear measurements with DEM-derived wear-intensity distributions, providing a valuable experimental reference for evaluating numerical wear-modelling approaches.

No cohesive-force model was activated, and the particulate charge was therefore treated as non-cohesive. As the model consisted of a single particulate population, contact parameters were defined for particle–particle and particle–steel interactions. Separate ore–ball interactions were not considered.

Table 3. DEM contact-model and interaction parameters

Parameter category	Interaction/property	Value
Contact model	Normal and tangential model	Hertz–Mindlin
Normal interaction	Elastic response	Nonlinear Hertzian contact
	Collision damping	Restitution-based damping
Tangential interaction	Tangential response	Incremental Mindlin-type frictional response
	Sliding limit	Coulomb friction criterion
Coefficient of restitution	Particle–particle	0.30
	Particle–steel	0.50
Static-friction coefficient	Particle–particle	0.50
	Particle–steel	0.50
Rolling-friction coefficient	Particle–particle	0.10
	Particle–steel	0.10
Cohesion	Cohesive-force model	Not activated
Particle material	Density	7850 kg/m^3
	Shear modulus	10 MPa
	Poisson's ratio	0.30
Steel boundary	Density	7850 kg/m^3
	Elastic modulus/shear modulus	-
	Poisson's ratio	-
Numerical setting	Integration timestep	2.0 x 10^{-5} s
Spatial setting	Grid-discretisation size	40 mm

2.1.3. Simulation timestep and data-acquisition procedure

The mill was operated at a rotational-speed magnitude of 15 rpm for five complete revolutions. The corresponding total simulated time was calculated as;

$$N_{\mathrm{rev}} = \frac{t_{\mathrm{sim}} n_{\mathrm{rpm}}}{60} \tag{1}$$

where N_{rev} is the number of mill revolutions, t_{sim} is the simulated time in seconds, and n_{rpm} is the rotational speed in revolutions per minute. For N_{rev}= 5 and n_{rpm}=15 rpm, the total simulated time was:

$$t_{\text{sim}} = \frac{60N_{\text{rev}}}{n_{\text{rpm}}} = \frac{60\ x\ 5}{15} = 20s \quad (2)$$

The DEM calculation was performed using a fixed integration timestep of:

$$\Delta t = 2.0 \times 10^{-5}\ \text{s} \quad (3)$$

This resulted in approximately 1.0×10^6 numerical integration steps over the complete 20 s simulation. The simulation does not contain a separately defined initial transient period or an independently selected steady-state data-acquisition interval. Consequently, the cumulative normal and tangential contact-energy outputs analysed in this study correspond to the complete five-revolution simulation. A formal steady-state convergence assessment based on the stabilisation of mill torque, power draw, charge kinetic energy or collision-energy rate was not conducted. The term "steady-state operation" is therefore avoided, and the results are described as cumulative energy distributions obtained over the investigated five-revolution interval.

The global cumulative normal and tangential energies were recorded at 4 s intervals, corresponding to one complete mill revolution at 15 rpm. For the spatial analysis, cumulative contact-energy values were extracted from the mill surface elements at the end of the 20 s simulation. The resulting energy distributions therefore represent all five revolutions, with no initial revolutions excluded from the analysis. Physical wear and progressive geometry updating were disabled during the DEM calculation. Consequently, the shell and lifter mesh remained unchanged throughout the simulation, and no geometry-update interval was applied. The calculated wear-depth field was obtained during post-processing by applying the energy-equivalent Archard formulation to the cumulative contact-energy values recorded on the original fixed geometry.

Using the inferred equivalent particle diameter of 48.46 mm, the estimated Rayleigh time is 2.30×10^{-3} s, corresponding to an integration timestep of approximately 0.87% of the Rayleigh time. Although this provides a numerical consistency check, independent timestep convergence was not established. Moreover, no independent timestep-sensitivity simulation was performed. Possible sensitivity of particle overlap, collision duration, and calculated contact-energy magnitude to the selected timestep is therefore acknowledged as a numerical limitation of the present study.

2.1.4. Archard wear formulation

The prediction of volumetric material loss on the lifter surfaces relies on a phenomenological approach derived from Archard's classic wear equation (Archard, 1953). Originally formulated to describe sliding wear, the classical Archard law postulates that the volume of removed material is directly proportional to the normal contact force and the sliding distance, and inversely proportional to the hardness of the wearing material (Archard & Hirst, 1956).

However, in the context of Discrete Element Method (DEM) simulations of tumbling mills, the interactions between the charge (ore and grinding media) and the lifters are highly dynamic, involving both severe normal impacts (cataracting) and continuous tangential abrasion (cascading). Consequently, the classical force-distance formulation is typically adapted into an energy-dissipation framework to better capture the transient nature of these particle-wall collisions (Kalala et al., 2005; Xu et al., 2018).

Archard's wear law describes wear volume as a function of force, sliding distance, material hardness, and a dimensionless wear coefficient:

$$V = \frac{K \cdot F \cdot s}{H} \quad (4)$$

where V is wear volume in mm^3, K is simensionless wear coefficient, F is contact force in Newtons (N), s is sliding distance in meters (m), H is Brinell hardness of material (H=875).

Given that DEM provides energy instead of force and distance explicitly, the equation is adapted by expressing:

$$F = \frac{E}{s} \quad (5)$$

Substituting into the original equation:

$$V = \frac{K \cdot E}{H} \quad (6)$$

For both normal and shear contributions, the equation becomes:

$$V_{\text{total}} = \frac{K_n \cdot E_n + K_s \cdot E_s}{H} \quad (7)$$

where K_n is normal wear coefficient, K_s is shear wear coefficient, E_n is energy from normal forces (Joules), E_s is energy from shear forces (Joules).

2.1.5. Wear coefficients

The normal and tangential wear coefficients, K_n and K_s, respectively, were introduced within the energy-equivalent Archard formulation to relate DEM-derived normal and tangential contact energies to the estimated volumetric loss of liner material. The coefficients were selected as effective, case-specific weighting parameters, with their selection informed by an indicative industrial wear reference and the relative contributions of normal and tangential contact energies obtained from the DEM simulation. The basis of the reference wear estimate and the adopted coefficient values are detailed below. An indicative annual lifter-wear reference was estimated using industrial operating information and a nominal specific-wear factor of 14.6203 mg/kWh. The reference operating conditions comprised a mill power of 1600 kW and an annual operating duration of 6180.48 h. Under the assumption that the specific-wear factor is expressed in mg/kWh, the corresponding annual mass loss is calculated as: $14.6203 \times 1600 \times 6180.48 \times 10^{-6} = 144.58$ kg/year

The specific-wear factor represents an industry-informed engineering assumption rather than a direct measurement of material loss from the simulated mill. The original supporting plant records were not retained for independent verification. Therefore, the resulting annual mass loss was adopted as a nominal reference for assessing the scaling of the energy-equivalent wear formulation and should not be interpreted as independent experimental validation of the DEM predictions.

For the investigated mill configuration, comprising 24 lifters operating at 15 rpm for 6180.48 h/year, the reference corresponds to an average mass loss of approximately 1.083×10^{-3} g per lifter per revolution. Alternative combinations of normal and tangential energy-weighting coefficients were examined to evaluate the relative contributions of the two contact-energy components. The coefficient pair adopted for the investigated operating condition is given below:

$$K_n = 7.0 \times 10^{-5}, \quad K_s = 9.0 \times 10^{-5} \quad (8)$$

The adopted coefficients, $K_n = 7.0 \times 10^{-5}$ and $K_s = 9.0 \times 10^{-5}$, represent one case-specific combination of phenomenological energy-weighting parameters considered within the proposed formulation. Their selection was informed by the nominal industrial wear reference and the relative contributions of normal and tangential contact energies obtained from the DEM simulation. Since a single aggregate wear reference provides only one independent constraint on the combined energy-weighted response, it cannot uniquely determine both coefficients. Accordingly, the selected pair is not regarded as a mathematically unique or globally optimal solution, but rather as a representative parameter combination adopted consistently for the investigated operating condition.

2.1.6. Archard formulation and analytical constraints

To translate these particle-scale collision events into a mathematically tractable predictive framework, this study adopted an energy-based adaptation of Archard's wear law. Classical Archard wear is fundamentally governed by sliding abrasion and is expressed as a function of normal force and sliding distance (F.s). Because DEM outputs energy dissipation directly, the mechanical work term was approximated as $E \approx F.s$, leading to the modified formulation: Eq. 7.

It must be explicitly acknowledged that applying Archard's framework to normal impact energy (E_n) is a mathematical simplification. True normal impacts lack a sliding distance and induce wear via surface fatigue and plastic deformation rather than abrasive micro-cutting. Therefore, this model functions strictly as an energy-equivalent phenomenological analog.

The normal and tangential wear coefficients were adopted as case-specific weighting parameters, with their overall scaling informed by the nominal annual wear reference described in Section 2.1.5. Because this reference represents an aggregate estimate rather than independent measurements of impact- and abrasion-induced material loss, the coefficient pair cannot be uniquely identified. The resulting wear

estimates are therefore interpreted within the assumptions of the energy-equivalent formulation rather than as independently validated predictions of absolute material loss.

2.1.7. Model assumptions

The grinding mill is represented as a hollow cylinder of 4 meters in diameter and 6 meters in length. 24 uniformly spaced lifters, arranged circumferentially, each extending along the full height. Each triangle (mesh face) from the DEM simulation is associated with a centroid coordinate (x_i, y_i, z_i). These centroids are used to assign each triangle to a specific lifter region and axial height.

Energy data obtained from the DEM simulations represent cumulative per-triangle contact energy. Assuming that energy values reliably represent work done through friction and impact, they are treated as proxies for Eq. 5. This allows Archard's law to be applied directly and removes the dependency on explicitly resolving contact durations or trajectories, which are often noisy or variable in DEM simulations. Thus, in Eq. 7, per triangle: K_n and K_s are the wear coefficients for normal and shear energy components, respectively; $E_{n,i}$ and $E_{s,i}$ are the energies (Normal & Shear) transferred to the surface and H is the Brinell hardness of the material.

2.2. Post processing

Post-processing was carried out using Python-based numerical tools following a structured workflow:

1. Near-shell filtering: Only particles located within the outer 10% of the mill radius were retained to isolate lifter–charge interactions.
2. Lifter identification: Particle contacts were assigned to individual lifters based on angular position. To translate the discrete, highly stochastic energy spectra obtained from the DEM mesh into a one-dimensional regional representation, the 3D cylindrical coordinate data (r, θ, z) of the mill internal surface must be systematically unwrapped and projected onto a localized 2D morphological profile.
3. Non-uniform regional segmentation: Rather than treating the lifter and shell as a single continuous curve, the geometry of each of the 24 lifter sections (spanning 15° of the mill circumference) was subdivided circumferentially into five physically defined regions (Powell, 1991; Hlungwani et al., 2003; Bian et al., 2017; Pural and Boylu, 2025) (Fig. 1):
   - Leading Face Plate (Bridge_L): The section of the mill shell immediately preceding the lifter. This zone primarily experiences sliding friction from the toe of the charge and secondary impacts.
   - Leading Face (Side_L): The aggressive 60° impact zone facing the direction of rotation. This region intercepts the high-energy, cataracting trajectories of heavy grinding media, making it heavily dominated by orthogonal normal forces (E_n).
   - Top: The apex of the lifter, which serves as a highly abrasive transition zone where particles crest the lifter under severe compressive loading before cascading.
   - Trailing Face (Side_R): The sheltered, low-pressure descent angle of the lifter. Wear in this region is almost exclusively driven by low-velocity, continuous tangential shear (E_s) as material cascades downward.
   - Trailing Face Plate (Bridge_R): The section of the mill shell situated in the wake of the lifter, subject to continuous rolling and sliding abrasion from the bulk charge bed.

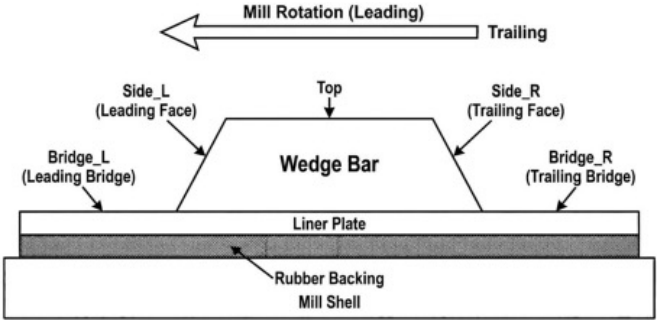


Fig. 1. Cross-sectional subdivisions of the wedge bar lifter surface. Mathematically partitioned into five physically and kinematically distinct boundary regions. This segmentation is critical, as the collision physics – and consequently the ratio of normal to shear energy dissipation – vary drastically across geometric inflection points

Bridge regions were intentionally defined as narrow angular sectors (~1°) to isolate transition zones at lifter entry and exit, while side and top regions occupied broader spans corresponding to sustained contact and energy transfer.

4. Energy aggregation: Impact and shear energies were accumulated within each region and averaged over time.
5. Statistical condensation: Median energies across all lifters were extracted for each region, yielding robust representative values that are less sensitive to transient extreme events.

This process resulted in five discrete data points describing the spatial distribution of energy along a representative lifter.

2.2.1. Lifter identification

To assign triangles to lifters, we calculate the angular position θ of each triangle using its (x_i) and (y_i) coordinates:

$$\theta_i = \arctan 2\,(y_i, x_i) \tag{9}$$

Since the domain is circular, $\theta_i \in (-\pi, \pi]$. We shift the domain to [0, 2π):

$$\theta_i{}^{+} = (\theta_i + 2\pi, \text{if } \theta_i < 0 \quad ; \quad \theta_i, \text{otherwise}) \tag{10}$$

The 24 lifters are spaced at 15° intervals, i.e., $\frac{2\pi}{24} = \frac{\pi}{12}$

Each triangle is mapped to lifter L_k such that:

$$k = \left\lfloor \frac{12}{\pi} \cdot \theta_i^{+} \right\rfloor, \quad \text{for } k = 0,1,\ldots,23 \tag{11}$$

Thus, every triangle is grouped by angular segment into one of 24 lifter zones.

Each triangle's (z_i) coordinate is used to determine its height segment along the lifter. Given the total height is 6 meters, the Z-axis is divided into bins (e.g., 0.150 m intervals for 40 layers). This enables vertical wear profiling:

$$h_{\text{bin}} = \left\lfloor \frac{z_i + 3}{\Delta z} \right\rfloor, \quad \text{where } \Delta z = 0.15\ m \tag{12}$$

Here, the origin is centered at z=0, so we shift it to a positive range.

2.2.2. Pseudo data processing

A spatial classification algorithm was implemented in Python (NumPy, pandas) to assign each triangle to a lifter ID and vertical segment. The centroid angle $\theta_i = \arctan 2\,(y_i, x_i)$ was used to divide the 360° circumference into 24 lifter sectors. Vertically, the Z-axis (–3 to +3 m) was binned in 0.150 m intervals, yielding 40 segments. This 2D classification by angle and height enabled the mapping of all mesh elements to lifter positions in 3D space, forming the basis for lifter-specific wear, energy, and force analyses.

This spatial classification framework:

- Ensures geometric consistency with actual lifter layout
- Complies with cylindrical symmetry
- Provides traceability from raw triangle mesh to component-level diagnostics
- Enables consistent filtering (e.g., all triangles on Lifter 17, lower third)

By using the angular segmentation method instead of simple X-Y slicing, we avoid distortion and ensure physical realism in modeling.

2.2.3. Axial discretisation and end-wall treatment

The axial-bin index of surface element i was calculated as:

$$h_i = \min\left\{39, \left\lfloor \frac{z_i + 3.0}{\Delta z} \right\rfloor\right\}, \quad h_i \in \{0,1,\ldots,39\} \tag{13}$$

The first axial bin covered the interval from −3.00 to −2.85 m, while the final bin covered the interval from 2.85 to 3.00 m. These two outermost bins were adjacent to the flat axial end walls. The surface elements located within these bins were retained in the analysis so that the complete axial loading distribution was represented.

The five-region polynomial representation was applied to the circumferential liner and lifter surfaces rather than to the axial end-wall surfaces. Nevertheless, interactions with the flat mill ends influenced the energy recorded on nearby liner and lifter elements. The elevated energies observed near z=±3.0 m were therefore interpreted as end-wall-related boundary effects rather than as uniform behaviour along the complete lifter length.

The primary regional energy calculations included all 40 axial bins. A separate central-domain polynomial was not constructed. Consequently, the reported regional energies incorporate both the central mill response and the influence of the end-wall-adjacent zones. Axial variations and end-wall effects are examined separately in the Results and Discussion section.

2.3. Available fitting techniques

Several regression approaches were evaluated for approximating the discrete regional energy data:

- Ordinary Least Squares (OLS): Closed-form, interpretable, and stable for low-order polynomials (Draper and Smith, 1998).
- Weighted Least Squares (WLS): Incorporates region-dependent confidence weights (Draper and Smith, 1998).
- Robust regression: Reduces sensitivity to extreme collision events (Huber, 1981; Rousseeuw and Leroy, 1987).
- Regularized regression (Ridge/Lasso): Controls coefficient variance in multi-parameter datasets (Hoerl and Kennard, 1970; Tibshirani, 1996).
- Nonlinear least squares: Enables constrained or physics-informed models.
- Gaussian Process Regression: Offers uncertainty quantification but requires larger datasets (Rasmussen and Williams, 2006).

Given the limited number of representative points and the need for interpretability, OLS was selected as the most appropriate method.

2.4. Choice of fitting method

A cubic polynomial was selected as the lowest-order function capable of reproducing the asymmetric spatial behavior observed in both impact and shear energy profiles. Lower-order polynomials were insufficient to capture the observed curvature, while higher-order fits risk overfitting given the limited dataset. Ordinary least squares regression was therefore adopted due to its transparency, analytical tractability, and reproducibility, following the standard matrix formulation described by Draper and Smith (1998).

The general polynomial form is given by:

$$E(x) = ax^3 + bx^2 + cx + d \tag{14}$$

where x denotes the normalised ordinal coordinate of the five lifter regions (0, 0.25, 0.50, 0.75 and 1.00), rather than their actual physical lengths.

2.5. Application of the fitting procedure

For each energy mode (impact and shear), the regression problem was formulated as a linear system (Chapra & Canale, 2010):

$$y = Xc + \epsilon \tag{15}$$

where $c = [ab\ cd]^T$ is the coefficient vector. The least-squares solution minimizing the sum of squared residuals is obtained as (Draper & Smith, 1998):

$$c = (X^T X)^{-1} X^T y \tag{16}$$

The resulting coefficients describe the spatial energy distribution along the lifter surface.

2.6. Fitting accuracy and error assessment

Model performance was evaluated using the coefficient of determination (R^2) and residual analysis. The impact energy fit achieved R^2=0.99, while the shear energy fit yielded R^2=0.94. Since four

polynomial coefficients were fitted to five regional observations, only one residual degree of freedom remained. The corresponding adjusted R^2 values were approximately 0.96 and 0.76, respectively, indicating good within-case agreement but not independently established predictive robustness.

2.7. Generalization strategy

The fitted coefficients represent baseline values corresponding to the simulated operating condition. For future generalisation, each coefficient could be expressed as an affine function of normalised physical variables, relying on a first-order Taylor series expansion approach for sensitivity analysis (Chapra & Canale, 2010). The proposed sensitivity matrices remain conceptual and require additional DEM conditions for coefficient estimation and validation. This leads to the matrix formulation proposed in this study:

- Critical speed ratio (n)
- Geometry index combining lifter height and face angle (g)
- Filling degree (J)
- Load intensity (L)

This leads to the matrix formulation:

$$c = Mu, \quad u = [1, n - n_0, g - g_0, J - J_0, L - L_0]^T \tag{17}$$

Separate sensitivity matrices are defined for impact and shear. While the present study identifies baseline coefficients from a single DEM scenario, extension to multi-condition datasets enables estimation of sensitivity matrices via least-squares regression.

The resulting generalized polynomial, representing the summation of baseline trends and linear perturbations, is defined as:

$$E(x) = \sum_{k=0}^{3}\left(A_k + \sum_i A_{k,i}\Delta p_i\right)x^{3-k} \tag{18}$$

3. Results and discussion

3.1. DEM results

3.1.1. Mesh sizing

The geometric representation of the tumbling mill (4000 mm in diameter and 6000 mm in length) was imported into the DEM environment as a Standard Tessellation Language (STL) file. To facilitate the highly localized tracking of particle-wall interactions, the internal mill shell and the 24 lifters were discretely represented as a high-resolution triangulated surface mesh. The DEM exports comprised 20,901 surface-point-force records and 15,872 spatial-energy records indexed by triangle identifiers. Based on the macroscopic mill geometry, this corresponds to an average surface area of approximately 6,000 mm^2 per element (equivalent to an average edge length of ~115 mm), ensuring that micro-level wear patterns on specific lifter faces could be mapped accurately into the 150 mm axial bins without spatial aliasing.

3.1.2. Distribution of surface energy

The DEM simulations yielded a highly resolved spatial dataset by discretizing the internal mill liner into a triangulated surface mesh, where each element recorded cumulative normal (E_n) and shear (E_s) energy dissipation during the operation. Statistical analysis of these energy fields revealed a pronounced right-skewed, heavy-tailed distribution. The vast majority of surface triangles experienced low-intensity, frequent interactions, registering total cumulative energies below 200 J. However, a highly localized subset of mesh elements sustained severe impact energies approaching 1500 J. Threshold filtering quantified this attenuation of impact frequency: 10,556 surface triangles fell within the 100 J energy threshold (averaging 172.18 J in normal energy and 94.30 J in shear), rapidly decaying to only 243 triangles registering at the 800 J threshold (averaging 385.40 J normal and 666.32 J shear) (Table 4). Isolated by energy component confirmed that normal impact energies exhibited a significantly broader statistical dispersion, while shear energies remained heavily concentrated in lower magnitude regimes. This highlights that shear acts primarily as a sustained, low-intensity abrasive mechanism,

whereas the high-variance tail of normal energy (> 600 J) represents the acute mechanical fatigue responsible for localized macro-spalling. Analysis of the archived cumulative energy histories showed relatively stable increments during revolutions 2–5, with coefficients of variation of 0.59% for normal energy and 0.83% for shear energy. However, the first revolution exhibited substantially higher energy increments, and the five-revolution results should not be interpreted as independently verified steady-state conditions.

Table 4. Attenuation of high-energy contact events and transition of force dominance across critical energy thresholds

Cumulative Energy Threshold, E_{th} (J)	Affected Mesh Elements (N)	Relative Frequency (%)	Mean Normal Energy, $\bar{E}_n$ (J)	Mean Shear Energy, $\bar{E}_s$ (J)	Energy Ratio $\bar{E}_n$ / $\bar{E}_s$	Dominant Modality
≥ 100	10,556	100.0%	172.18	94.30	1.83	Impact
≥ 200	5,903	55.9%	226.91	125.37	1.81	Impact
≥ 400	1,510	14.3%	369.48	242.64	1.52	Impact
≥ 800	243	2.3%	385.40	666.32	0.58	Shear
≥ 1600	0	0.0%	-	-	-	None

3.1.3. Energy dominance points

To rigorously evaluate localized wear mechanisms, a spatial classification algorithm was applied to determine force dominance across the mill geometry, evaluating the binary condition $E_{s,i} > E_{n,i}$ versus $E_{n,i} > E_{s,i}$ for each discrete triangle. This mapping exposed distinct, physics-consistent wear regimes dictated by charge kinematics. Shear-dominated interactions were systematically localized at the upper and lower axial boundaries of the cylindrical domain (Fig. 2), as well as on the trailing faces and extreme edges of the lifters. These regions mechanistically correspond to zones where rotational lift and particle sliding are maximal. In contrast, normal-force dominance was densely concentrated in the central axial zone and on the leading faces of the lifters (Maleki-Moghaddam et al., 2013) (Fig. 3). This spatial trend physically aligns with the macro-dynamics of the mill toe zone, where cataracting media undergoes direct, high-velocity deceleration against the liner (Fig. 4). Applying a > 600 J critical energy threshold identified 528 surface triangles suffering from severe stress concentrations, pinpointing them as high-risk initiation sites for localized structural degradation.

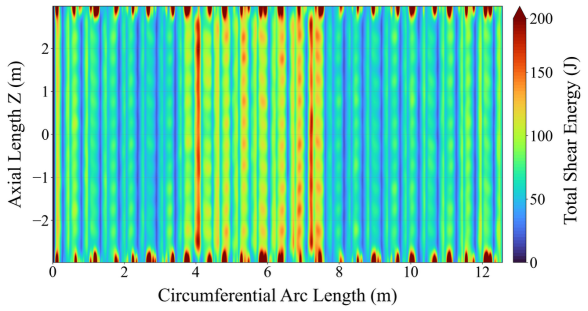


Fig. 2. Mapping of shear-dominated interactions within the unrolled mill geometry

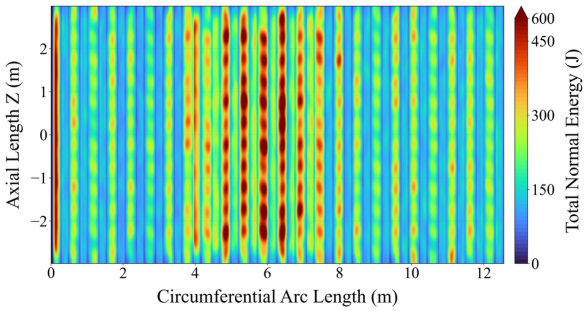


Fig. 3. Mapping of normal-force dominance across the mill liner

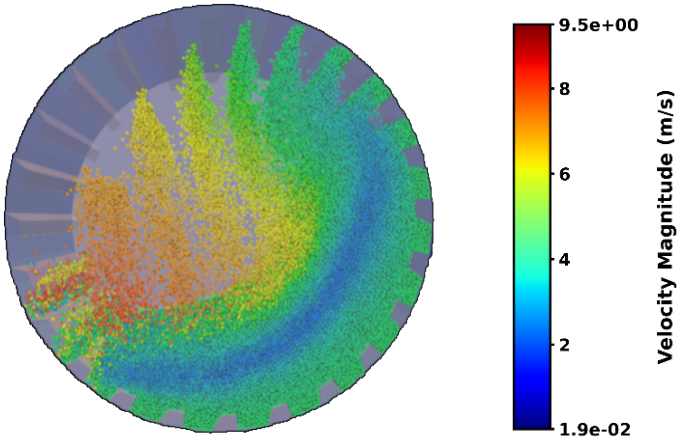


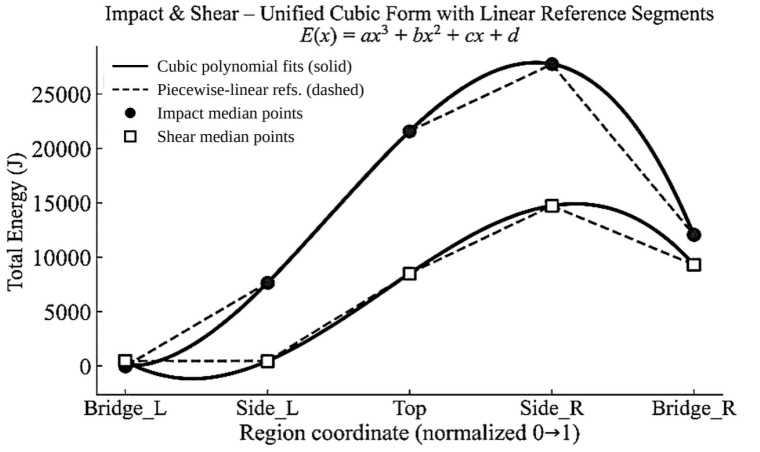
Fig. 4. Macro-dynamic charge behavior at the mill toe zone

3.2. Discussion

The fitted polynomial functions accurately reproduce the median impact and shear energy distributions across the defined lifter regions. High coefficients of determination (R^2=*0.99* for impact and R^2=*0.94* for shear) indicate that the polynomial form captures the dominant spatial trends present in the DEM data.

Distinct differences between impact and shear coefficients are observed, despite both being influenced by the same physical parameters. This divergence is expected, as impact energy is governed primarily by normal collision dynamics (Soleymani et al.2022) and charge detachment velocity, whereas shear energy arises from sustained sliding contact and frictional dissipation along the lifter surface. These differences reflect the distinct normal and tangential contact mechanisms under the investigated operating condition; sensitivities to changing operating parameters were not evaluated.

Although the present coefficients were obtained from a single DEM simulation, the agreement between the regional observations and fitted curves supports the descriptive capability of the proposed framework for the investigated case (Xu et al. 2018; Wang et al. 2025). Importantly, the formulation enables direct comparison between impact-dominated and shear-dominated wear mechanisms within a unified analytical structure (Fig. 5).



Coefficient	Polynomial term	Impact Value	Shear Value
a	Cubic term	-1.50e+05	-1.05e+05
b	Quadratic term	1.63e+05	1.43e+05
c	Linear term	-6.75e+02	-2.93e+04
d	Intercept	-3.79e+01	4.50e+02

Fig. 5. Cubic polynomial fits (solid curves) and piecewise-linear reference segments (dashed lines) representing the median normal (impact) and tangential (shear) contact-energy distributions across the five predefined lifter regions

Filled circles and open squares denote the DEM-derived impact and shear median values, respectively. The horizontal axis represents normalised regional position rather than physical distance along the lifter surface. The corresponding cubic polynomial coefficients are provided in the accompanying table.

When evaluating the DEM-based wear profile, the geometry exhibits severe spatial noise and jagged surface artifacts. Rather than treating this as a computational error, this noise must be understood as the true, highly discretized representation of tumbling mill kinematics. Because DEM models individual, transient particle collisions, the DEM-predicted wear depth inherently captures extreme, localized material loss anomalies—highlighting localized peaks in the energy-equivalent wear indicators.

This is quantitatively proven by the localized wear depth contour (Fig. 6), which serves as our statistical baseline. The distribution of spatial deformation is heavily right-skewed and fundamentally bifurcated. An overwhelming bulk of the mesh (a large proportion of the recorded surface locations) registers minimal localized wear depth, representing the continuous, uniform, but shallow abrasive sliding that dominates the trailing faces. Conversely, the distribution exhibits a critical "heavy tail" of fewer than 500 elements that capture severe, deep localized gouging. Relying purely on an arithmetic average of this wear depth would be a critical physical error; the massive volume of shallow trailing-face contacts would mathematically dilute the aggressive, deep localized trenching on the leading face that actually dictates component failure (Kalala et al., 2005; Boemer and Ponthot, 2017; Xu et al., 2018).

To bridge the gap between these discrete simulation craters and the experimentally observed physical reality of a continuously wearing cast-steel lifter (Kalala et al., 2005; Yahyaei et al., 2009; Boemer and Ponthot, 2017; Xu et al., 2018), spatial smoothing is required (Fig. 7). After deriving the localized volumetric loss via the dual-coefficient Archard approach ($K_n = 7.0 \times 10^{-5}$, $K_s = 9.0 \times 10^{-5}$), a continuous cubic polynomial regression is applied across the unrolled lifter perimeter to predict the final geometric recession.

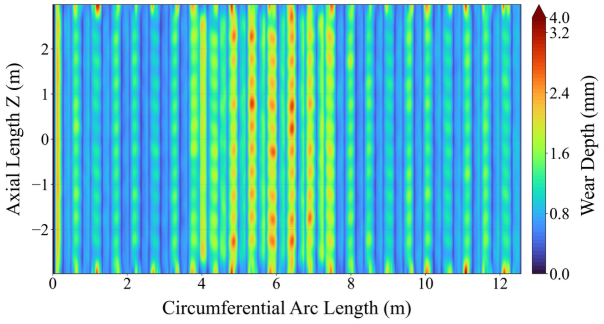


Fig. 6. Raw DEM unrolled wear profiles

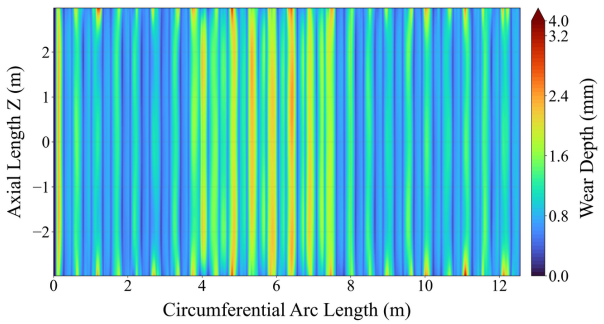


Fig. 7. Smoothed unrolled wear profiles with polynomial fit

The distinct difference between the raw and smoothed profiles highlights the physical boundary between isolated impact events and long-term mechanical degradation.

The DEM-based profile isolates the exact spatial coordinates of catastrophic media strikes. The distinct, jagged spikes in wear depth on the Leading Face and Top Edge directly reflect the heavy-tail statistical distribution of extreme deformation.

The Polynomial fitting based wear profile, accurately represents macroscopic geometric recession over time. The cubic fit filters the localized high-frequency cratering while strictly preserving the asymmetric nature of the wear mechanisms. It successfully captures the deep, concaving wear trench on the Leading Face (where impact drives severe depth) and the gradual, uniform abrasive thinning on the Trailing Face (where shear drives shallow, widespread wear). Ultimately, while the raw DEM wear depth provides the essential forensic baseline for individual collision severity, the polynomial fit provides a simplified representation of the spatial wear trends, while long-term geometric evolution remains to be validated.

Despite the predictive capabilities demonstrated by the proposed numerical framework, it is imperative to critically evaluate the inherent assumptions and boundary conditions that constrain the model. The extrapolation of localized Discrete Element Method (DEM) energy spectra into long-term volumetric wear introduces several mathematical and physical limitations that must be addressed to contextualize the fidelity of the results.

A primary limitation of this study stems from the fundamental reliance on an energy-equivalent adaptation of Archard's wear formulation ($V_{total} = (K_n E_n + K_s E_s) / H$). While this scalar transformation is computationally tractable and widely accepted for macro-scale predictions, it inherently simplifies complex, micro-mechanical tribological phenomena. The empirical wear coefficients for impact ($K_n = 7.0 \times 10^{-5}$) and shear (9.0×10^{-5}) are treated as linear, time-invariant constants. In physical milling environments, however, lifter materials undergo dynamic surface alterations such as strain hardening, localized thermal softening, and corrosive degradation (particularly in wet milling scenarios). By homogenizing these micro-structural transitions into static coefficients, the model may under-predict wear resistance variations during the intermediate stages of the lifter's life cycle.

The methodology relies on capturing energy spectra and scaling these localized interactions over extended temporal cycles to predict cumulative mass loss. Real-world mill lifter wear, however, is a highly transient and non-linear process. As the leading face profile recedes due to continuous high-energy impacts, the face angle degrades, directly altering the charge trajectory and subsequently shifting the internal energy distribution. While our polynomial regression smooths the spatial transitions across the five defined geometric zones (Leading Face Plate, Leading Face, Top, Trailing Face, and Trailing Face Plate), extrapolating discrete time-steps over thousands of operating hours without continuous, dynamic mesh reconstruction risks overestimating impact dominance in the latter stages of the lifter lifespan, where shear forces typically begin to dominate. Crucially, this static temporal scaling and assumption of uniform geometric extrapolation directly dictate the spatial distribution of the predicted material loss. As the model aggregates these discrete energy spectra into volumetric recession without adaptive mesh feedback, the resulting geometric degradation manifests as highly localized, non-uniform wear bands across the lifter's geometry (Fig. 8).

While acknowledging the inherent phenomenological constraints outlined, the proposed numerical framework delivers substantial predictive utility for the optimization of industrial comminution circuits. By decoupling normal (E_n) and shear (E_s) energy fields into physically interpretable regional

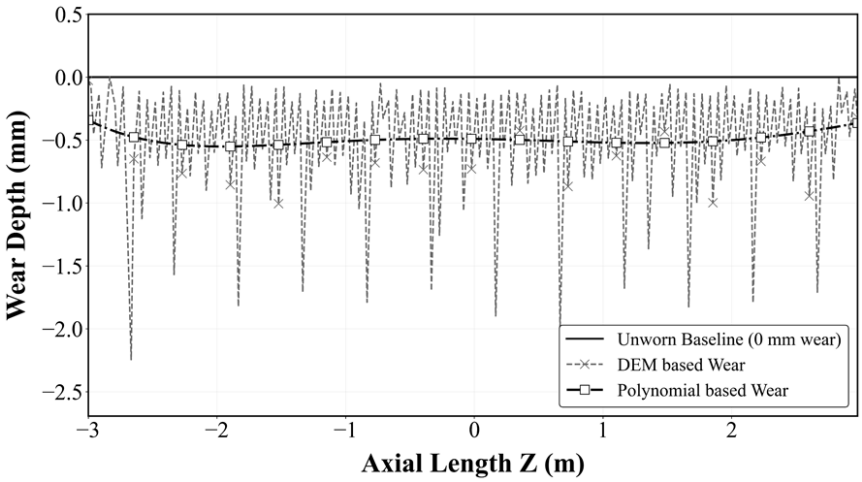


Fig. 8. DEM-based versus polynomial-fitting wear depths

descriptors, the method converts discrete mesh-level collision data into a compact analytical form that can be compared across lifter geometries and operating conditions.

The primary application of this spatial energy mapping lies in iterative liner design. Traditional lifter design often relies on empirical trial-and-error, which is costly and requires months of physical downtime to evaluate. It's potential integration with generalized predictive models. Separating the total dissipated energy into normal-impact and tangential-shear components enables impact-dominated and abrasion-dominated regions to be analysed independently. This distinction is important because lifter height, face angle, spacing, mill speed, and filling degree can strongly influence charge trajectory and redistribute collision energy over the liner surface (Powell, 1991; Bian et al., 2017; Cleary and Owen, 2018; Jauhar et al., 2026a).

In this context, the fitted polynomial coefficients should be interpreted as reduced-order descriptors rather than universal constants. With a sufficiently broad DEM dataset, these coefficients could be related to operating and design variables using regression, response-surface modelling, or interpretable machine-learning methods. This provides a pathway toward generalized liner-wear models capable of predicting how changes in operating conditions or lifter geometry modify the balance between impact and shear energy, consistent with recent work on machine-learning-based liner-wear prediction and interpretable SAG mill energy-spectrum analysis (Pural et al., 2024; Jauhar et al., 2026a).

Therefore, the long-term value of the proposed framework is not limited to reproducing a single simulated wear profile. Rather, it establishes a physically interpretable bridge between DEM simulations, fitting-based surrogate models, machine-learning generalization, and practical liner-design or maintenance strategies. Future application will require validation against measured liner profiles and multi-condition DEM simulations before quantitative industrial implementation.

Beyond initial design, the temporal scaling capabilities of the model provide a foundation for predictive maintenance scheduling. By translating discrete energy interactions into volumetric mass loss, plant operators can generate digital twins of their mill liners (Beloglazov and Plaschinsky, 2024).

4. Conclusions

A region-based analytical framework has been developed to represent DEM-derived impact and shear energy distributions on grinding mill lifters using a unified cubic polynomial form. By mapping energy spectra onto physically defined lifter regions and representing their spatial variation through polynomial coefficients, the approach bridges detailed DEM analysis with analytical tractability.

The current study is intentionally limited to a single DEM scenario and should be regarded as a proof-of-concept rather than a finalized predictive model. Future work will focus on extending the framework through multiple DEM simulations spanning a broader range of operating conditions, including variations in mill speed, lifter geometry, filling degree, and load intensity. Together with contact-parameter sensitivity tests, numerical convergence assessments, and independent liner-wear measurements, an expanded DEM dataset would enable evaluation of coefficient transferability and the development of more general predictive models.

Ultimately, the proposed methodology offers a promising pathway toward reducing reliance on repeated DEM simulations while retaining physical interpretability, providing a valuable tool for lifter design optimization and wear prediction.

Acknowledgments

A part of the results reported in this paper were presented at XX Balkan Mineral Processing Congress BMPC 2026 entitled "Numerical prediction of impact and shear energy profiles on mill lifters".

References

AKHONDIZADEH, M., FOOLADI MAHANI, M., REZAEIZADEH, M., MANSOURI, S., 2016. *Prediction of tumbling mill liner wear: Abrasion and impact effects.* Proceedings of the Institution of Mechanical Engineers, Part J: Journal of Engineering Tribology. 2016;230(10):1310-1320.

ALLEN, M., 2021. *Mining Energy Consumption 2021.* Engeco Pte Ltd.

ANSYS, 2025. *Ansys Rocky particle-dynamics simulation software. Available at: https://www.ansys.com/products/fluids/ansys-rocky (accessed 11 November 2025).*

AREKAR, C.A., 2004. *Real-Time Analysis with Development, Simulation and Validation of Discrete Element Method Models for Tumbling Mill Charge Motion and Liner Wear.* Thesis, Department of Mechanical Engineering, McGill University, Montreal, Canada.

AUSTIN, L., et al., 1986. *An improved simulation model for semi-autogenous grinding.* Powder Technology 47(3), 265–283.

BAILEY, C., et al., 2009. *What can go wrong in comminution circuit design*. In: Proceedings of the 10th Mill Operators' Conference, Adelaide, South Australia.

BANISI, S., & HADIZADEH, M., 2007. *3-D liner wear profile measurement and analysis in industrial SAG mills*. Minerals Engineering, 20(2), 132–139.

BATES, D.M., WATTS, D.G., 1988. *Nonlinear Regression Analysis and Its Applications.* John Wiley & Sons, New York.

BELOGLAZOV, I., PLASCHINSKY, V., 2024. *Development of model predictive control for the grinding process in SAG mills using DEM investigations of liner wear.* Materials 17(4), 795.

BIAN, X., WANG, G., WANG, H., WANG, S., LV, W., 2017. *Effect of lifters and mill speed on particle behaviour, torque, and power consumption of a tumbling ball mill: Experimental study and DEM simulation.* Minerals Engineering 105, 22–35.

BILGILI, E., 2024. *Population balance modeling of milling processes: Are we falsifying breakage kinetics and distribution via back-calculation methods?* Powders 3(2), 190–201.

BISHT, M.S., et al., 2024. *Heterarchical modelling of comminution for rotary mills: Part I – particle crushing along streamlines.* Granular Matter 26(4), 88.

BOEMER, D., PONTHOT, J.-P., 2017. *A generic wear prediction procedure based on the discrete element method for ball mill liners in the cement industry.* Minerals Engineering 109, 55–79.

BOND, F.C., 1961. *Crushing and grinding calculations, Part I. British Chemical Engineering 6, 378–385.*

BOUCHARD, J., LEBLANC, G., LEVESQUE, M., RADZISZEWSKI, P., GEORGES-FILTEAU, D., 2019. *Breaking down energy consumption in industrial grinding mills.* CIM Journal 10, 157–164.

BUENO, M.D.P., 2013. *Development of a Multi-Component Model Structure for Autogenous and Semi-Autogenous Mills.* Thesis.

CARVALHO, R., 2013. *Mechanistic Modelling of Semi-Autogenous Grinding.* PhD dissertation, Universidade Federal do Rio de Janeiro, Rio de Janeiro, Brazil.

CHAKRABORTY, J., RAMKRISHNA, D., 2011. *Population balance modeling of environment-dependent breakage: Role of granular viscosity, density and compaction. Model formulation and similarity analysis.* Industrial & Engineering Chemistry Research 50(23), 13116–13128.

CHAPRA, S. C., & CANALE, R. P., 2010. *Numerical Methods for Engineers.* McGraw-Hill.

CHEN, W., HAZELL, M., GROBLER, A., SHORE, T., MORKEL, F., 2023. *Leveraging digital tools for improving SAG mill operation for stable charge and near-real-time trajectory prediction. Presented at the SAG Conference, Vancouver, Canada.*

CLEARY, P. W., 2001. *Charge behaviour and power consumption in ball mills: Sensitivity to mill operating conditions, liner geometry and charge composition.* International Journal of Mineral Processing, 63(2), 79–114.

CLEARY, P., MORRISON, R., 2011. *Predicting patterns of slurry flow within and discharge from a three-dimensional pilot SAG mill.*

CLEARY, P., MORRISON, R., MORRELL, S., 2001. *DEM validation for a scale-model SAG mill.* In: Proceedings of the International Autogenous and Semiautogenous Grinding Technology Conference, pp. 191–206.

CLEARY, P.W., 1998. *Predicting charge motion, power draw, segregation and wear in ball mills using discrete element methods.* Minerals Engineering 11(11), 1061–1080.

CLEARY, P.W., et al., 2018. *Inclusion of incremental-damage breakage of particles and slurry rheology into a particle-scale multiphase model of a SAG mill.* Minerals Engineering 128, 92–105.

CLEARY, P.W., et al., 2020. *Advanced comminution modelling: Part 2 – mills.* Applied Mathematical Modelling 88, 307–348.

CLEARY, P.W., FRANKE, J., 2012. *Effect of laser-scanned geometry and liner wear on DEM modelling of mill performance for a full-scale three-dimensional SAG mill.* Canadian Institute of Mining, Metallurgy and Petroleum.

CLEARY, P.W., MORRISON, R., 2016. *Comminution mechanisms, particle-shape evolution and collision-energy partitioning in tumbling mills.* Minerals Engineering 86, 75–95.

CLEARY, P.W., MORRISON, R., MORRELL, S., 2003. *Comparison of DEM and experiment for a scale-model SAG mill.* International Journal of Mineral Processing 68(1–4), 129–165.

CLEARY, P.W., MORRISON, R.D., 2012. *Prediction of three-dimensional slurry flow within the grinding chamber and discharge from a pilot-scale SAG mill.* Minerals Engineering 39, 184–195.

CLEARY, P.W., MORRISON, R.D., DELANEY, G.W., 2018. *Incremental damage and particle size reduction in a pilot SAG mill: DEM breakage method extension and validation.* Minerals Engineering 128, 56–68.

CLEARY, P.W., OWEN, P., 2018. *Development of models relating charge shape and power draw to SAG mill operating parameters and their use in devising mill operating strategies to account for liner wear. Minerals Engineering 117, 42–62.*

CLEARY, P.W., OWEN, P., 2019. *Effect of operating-condition changes on the collisional environment in a SAG mill.* Minerals Engineering 132, 297–315.

CLEARY, P.W., SINNOTT, M.D., MORRISON, R.D., 2023. *Scale-up investigation of a pilot and industrial-scale semi-autogenous mill using a particle-scale model.* Minerals 13(12), 1490.

DAN, A., et al., 2023. *Multi-dimensional population balance model development using a breakage-mode probability kernel for prediction of multiple granule attributes.* Pharmaceutical Development and Technology 28(7), 638–649.

DAS, A., et al., 2022. *An efficient multiscale bidirectional PBM–DEM coupling framework to simulate one-dimensional aggregation mechanisms.* Proceedings of the Royal Society A 478(2261), 20220076.

DELANEY, G.W., et al., 2013. *Predicting breakage and the evolution of rock-size and shape distributions in AG and SAG mills using DEM.* Minerals Engineering 50–51, 132–139.

DOSTA, M., ANDRE, D., ANGELIDAKIS, V., CAULK, R. A., CELIGUETA, M. A., CHAREYRE, B., ... & WEINHART, T., 2024. *Comparing open-source DEM frameworks for simulations of common bulk processes.* Computer Physics Communications, 296, 109066.

DRAPER, N. R., & SMITH, H., 1998. *Applied Regression Analysis (3rd ed.). John Wiley & Sons.*

DUNNE, R., et al., 2001. *Design of the 40-foot-diameter SAG mill installed at the Cadia Gold Copper Mine.* Presented at SAG 2001, Vancouver, British Columbia, Canada.

FANGRONG, D., YANG, D., MUÑOZ, A., VALERY, W., VALLE, R., BONFILS, B., PLASENCIA, C., 2023. *Integrated mine-to-mill optimization of the Toromocho operation at Minera Chinalco, Perú.* Presented at the SAG Conference, Vancouver, Canada.

FARIA, P.M., TAVARES, L.M., RAJAMANI, R.K., 2014. *Population balance model approach to ball mill optimization in iron ore grinding. In: ABM Proceedings.*

FRANKE, J., CLEARY, P.W., SINNOTT, M.D., 2015. *How to account for operating condition variability when predicting liner operating life with DEM: A case study.* Minerals Engineering 73, 53–68.

FRANKE, J., CLEARY, P.W., SINNOTT, M.D., 2015. *How to account for operating-condition variability when predicting liner operating life with DEM: A case study.* Minerals Engineering 73, 53–68.

FUERSTENAU, D.W., ABOUZEID, A.-Z.M., 2002. *The energy efficiency of ball milling in comminution.* International Journal of Mineral Processing 67, 161–185.

GHASEMI, A., RAZI, E., BANISI, S., 2020. *Determining a lower boundary of elasticity modulus used in the discrete element method (DEM) in simulation of tumbling mills.* Advanced Powder Technology 31, 1365–1371. https://doi.org/10.1016/j.apt.2020.01.014.

GUTIERREZ, A.G., 2019. *Mineral movement simulation through the grates and pulp lifter in a SAG mill and evaluation of a new grate design using DEM.* Physicochemical Problems of Mineral Processing 55.

HERMOSILLA, R., et al., 2024. *SAG overload forecasting using a CNN physics-informed approach.* Applied Sciences 14(24), 11686.

HLUNGWANI, O., RIKHOTSO, J., DONG, H., MOYS, M.H., 2003. *Further validation of DEM modeling of milling: Effects of liner profile and mill speed. Minerals Engineering 16, 993–998.*

HOERL, A.E., KENNARD, R.W., 1970. *Ridge regression: Biased estimation for nonorthogonal problems.* Technometrics 12(1), 55–67.

HOGG, R., 1972. *Power relationships for tumbling mills.* AIME Transactions 252, 418–423.

HOLMBERG, K., KIVIKYTÖ-REPONEN, P., HÄRKISAARI, P., VALTONEN, K., ERDEMIR, A., 2017. *Global energy consumption due to friction and wear in the mining industry.* Tribology International 115, 116–139.

HU, Y., CHEN, W., LYU, B., OUYANG, C., LI, J., WU, D., 2027. *Coupling of wear sensor measurements with numerical modelling for grinding mill charge dynamics prediction.* Minerals Engineering 250, 110871. https://doi.org/10.1016/j.mineng.2026.110871.

HUBER, P.J., 1981. *Robust Statistics.* John Wiley & Sons, New York.

IRANNAJAD, M., FARZANEGAN, A., RAZAVIAN, S.M., 2006. *Spreadsheet-based simulation of closed ball-milling circuits.* Minerals Engineering 19(15), 1495–1504.

JAHANI CHEGENI, M., KOLAHI, S., 2020. *An investigation of the effect of shell-liner type on the performance of industrial SAG mills using DEM.* Journal of Mining and Environment 11(2), 387–404.

JAUHAR, T., CLEARY, P.W., WHEELER, C., CARR, M., ELLİS, D., CHALUP, S., 2026. *SAG mill design techniques and comprehensive design methodology.* Powder Technology, 470, 121998.

JAUHAR, T.A., BALASOORIYA, D., WILKS, B., CHALUP, S., CARR, M.J., WHEELER, C.A., ELLIS, D., 2026. *Investigating the influence of design and operational parameters on SAG mill energy spectra: A DEM and SHAP-based sensitivity analysis.* Chemical Engineering Research and Design, 227, 583–600.

JESWIET, J., SZEKERES, A., 2016. *Energy consumption in mining comminution.* Procedia CIRP 48, 140–145.

KALALA, J.T., BWALYA, M.M., MOYS, M.H., 2005. *Discrete element method modelling of evolving mill liner profiles due to wear. Part I: DEM validation.* Minerals Engineering 18(15), 1386–1391.

LARBI-BRAM, S., 2009. *A Study of Ore Breakage Characterization for AG/SAG Mill Modelling.* Julius Kruttschnitt Mineral Research Centre, Sustainable Minerals Institute, The University of Queensland, Brisbane, Australia.

LATCHIREDDI, S., MORRELL, S., 2003. *Slurry flow in mills: Grate-only discharge mechanism, Part 1.* Minerals Engineering 16(7), 625–633.

LEUNG, K., MORRISON, R., WHITEN, W., 1987. *An energy-based ore-specific model for autogenous and semi-autogenous grinding.* Presented at Copper '87, Santiago, Chile.

LI, H., 2020. *Dynamic Modeling and Simulation of SAG Mill Circuits with Pebble Crushing.* Department of Industrial and Materials Science, Chalmers University of Technology.

LOMMEN, S., SCHOTT, D.L., LODEWIJKS, G., 2014. *DEM speedup: Stiffness effects on behavior of bulk material.* Particuology 12, 107–112. https://doi.org/10.1016/j.partic.2013.03.006.

LOPEZ-PACHECO, A., 2012. *Mill mods save money.* CIM Magazine 7(5), 40–41.

MACPHERSON, A.R., TURNER, R.R., 1984. *Mineral processing plant design.* SME/AIME, New York.

MAGDALINOVIĆ, N., 1989. *A procedure for rapid determination of the Bond work index.* International Journal of Mineral Processing 27(1–2), 125–132.

MAKOKHA, A.B., MOYS, M.H., 2006. *Towards optimising ball-milling capacity: Effect of lifter design.* Minerals Engineering 19, 1439–1445.

MALEKI MOGHADDAM, M., ARGHAVANI, E., GHASEMI, A.R., BANISI, S., 2019. *Changing SAG mill liners type from Hi-Low to Hi-Hi at Sarcheshmeh Copper Complex based on physical and numerical modeling.* Journal of Mining and Environment 10.

MALEKI-MOGHADDAM, M., et al., 2014. *Optimization of the design of AG mill shell liners at the Gol-E-Gohar Concentration Plant.* Presented at the XXVII International Mineral Processing Congress.

MALEKI-MOGHADDAM, M., YAHYAEI, M., BANISI, S., 2013. *A method to predict shape and trajectory of charge in industrial mills.* Minerals Engineering 46–47, 157–166.

MALKHUUZ, G., ZARANTONELLO, A., SUPRYADI, A., JALDIN, O., ERDENEBAATAR, B., GANBOLD, M.U., 2023. *Optimization and continuous improvement of the Oyu Tolgoi concentrator.* Presented at the SAG Conference, Vancouver, Canada.

MCBRIDE, A.T., POWELL, M.S., 2006. *A structured approach to modelling SAG mill liner wear: Numerical modelling of liner evolution.* Presented at the Canadian Institute of Mining, Metallurgy and Petroleum Conference.

MEDINA, M., SOTOMAYOR, G., MANCHEGO, V., BONILLA, J., VALERY, W., VALLE, R., DUFFY, K., WANG, E., 2023. *Review and optimization of the Hudbay Constancia comminution circuit*. Presented at the SAG Conference, Vancouver, Canada.

MISHRA, B.K., RAJAMANI, R.K., 1992. *The discrete element method for the simulation of ball mills.* Applied Mathematical Modelling 16(11), 598–604.

MISHRA, B.K., RAJAMANI, R.K., 1993. *Numerical simulation of charge motion in ball mills: Lifter bar effect.* Mining, Metallurgy & Exploration 10, 86–90.

MOLLER, T.K., BROUGH, R., 1989. *Optimizing the performance of a rubber-lined mill.* Mining Engineering.

MORRELL, S., 1993. *The prediction of power draw in wet tumbling mills.* PhD thesis, The University of Queensland, Brisbane, Australia.

MORRELL, S., 2004. *A new autogenous and semi-autogenous mill model for scale-up, design and optimisation.* Minerals Engineering 17(3), 437–445.

MORRELL, S., 2019. *How to formulate an effective ore comminution characterization program.* In: Proceedings of MetPlant 2019.

MORRISON, R., CLEARY, P.W., 2004. *Using DEM to model ore breakage within a pilot-scale SAG mill.* Minerals Engineering 17(11–12), 1117–1124.

MORRISON, R.D., SHI, F., WHYTE, R., 2007. *Modelling of incremental rock breakage by impact for use in DEM models.* Minerals Engineering 20(3), 303–309.

MOYS, M.H., SKORUPA, J., 1993. *Measurement of the radial and tangential forces exerted by the load on a liner in a ball mill as a function of load volume and mill speed.* International Journal of Mineral Processing 37(3–4), 239–256.

NAPIER-MUNN, T., 2015. *Is progress in energy-efficient comminution doomed?* Minerals Engineering 73, 1–6.

NAPIER-MUNN, T.J., et al., 1996. *Mineral Comminution Circuits: Their Operation and Optimisation.* Julius Kruttschnitt Mineral Research Centre, The University of Queensland, Brisbane, Australia.

O2M TECHNOLOGIES, n.d. *MillSoft. Available at: https://www.o2mtech.com/Public/millsoft/ (accessed 3 December 2024).*

OLMEDO, S., RODRIGUEZ, M., 2023. *Increasing the Collahuasi SAG mill feed rate through optimisation of grinding media size: Methodology, strategy, and results.* Presented at the SAG Conference, Vancouver, Canada.

OROZCO, L.F., et al., 2019. *Discrete-element simulation of particle breakage inside ball mills: A two-dimensional model. arXiv:1901.07402.*

PAX, R.A., BEVAN, A., 2023. *Rapid diagnostics and observations of the internal operation of a SAG mill in the context of its grinding circuit.* Presented at the SAG Conference, Vancouver, Canada.

PEDERSEN, C., FALCIONI, L., JORDENS, A., KRYSTIA, C., COLLINS, D., YOUSEFFI, E., PRIDDY-DELGADO, N., 2023. *Using SAG mill vibration for advanced process-control strategies and monitoring liner improvements.* Presented at the SAG Conference, Vancouver, Canada.

PETRAKIS, E., STAMBOLIADIS, E., KOMNITSAS, K., 2017. *Identification of optimal mill operating parameters during grinding of quartz with the use of population balance modelling.* KONA Powder and Particle Journal 34, 213–223.

PETRAKIS, E., VAROUCHAKIS, E., KOMNITSAS, K., 2023. *Reliability of nonlinear modelling in predicting the size distribution of grinding products under different operating conditions.* Mining, Metallurgy & Exploration 40(4), 1265–1278.

POWELL, M. S., MCBRIDE, A. T., & MAINZA, A. N., 2006. *The influence of liner design on mill performance.* Minerals Engineering, 19(6–8), 739–745.

POWELL, M., SMIT, I., RADZISZEWSKI, P., CLEARY, P., RATTRAY, B., SCHAEFFER, L., 2006. *The selection and design of mill liners. In: Kawatra, S.K. (Ed.), Advances in Comminution.* Society for Mining, Metallurgy, and Exploration, pp. 331–376.

POWELL, M., VERMEULEN, L.A., 1994. *The influence of liner design on the rate of production of fines in a rotary mill.* Minerals Engineering 7, 169–183.

POWELL, M., WEERASEKARA, N.S., COLE, S., LAROCHE, R.D., FAVIER, J., 2011. *DEM modelling of liner evolution and its influence on grinding rate in ball mills.* Minerals Engineering 24, 341–351.

POWELL, M.S., 1991. *The effect of liner design on the motion of the outer grinding elements in a rotary mill.* International Journal of Mineral Processing 31(3–4), 163–193.

POWELL,M., 2025. *Any Shape Lifter. Available at: https://www.milltraj.com/file/videos/any_shape_lifter_detailed_demo_10_minutes.mp4 (accessed 12 May 2025).*

PURAL, Y.E., BOYLU, F., 2025. *Prediction and visualization of charge shape and ball trajectory in tumbling mills: a Python-based tool for liner design and operational optimizations.* Physicochemical Problems of Mineral Processing, 61(3), 204533.

PURAL, Y.E., LEDEZMA, T., HILDEN, M., FORBES, G., BOYLU, F., YAHYAEI, M., 2024. *Application of machine learning for generic mill liner wear prediction in semi-autogenous grinding mills.* Minerals 14, 1200.

QIU, X., et al., 2001. *Prediction of wear of mill lifters using the discrete element method.* Simulation 4, 262.

RADZISZEWSKI, P., TARASIEWICZ, S., 1993. *Simulation of ball charge and liner wear.* Wear 169(1), 77–85.

RASMUSSEN, C.E., WILLIAMS, C.K.I., 2006. *Gaussian Processes for Machine Learning.* MIT Press, Cambridge, MA.

ROUSSEEUW, P.J., LEROY, A.M., 1987. *Robust Regression and Outlier Detection.* John Wiley & Sons, New York.

ROYSTON, D., 2007. *Semi-autogenous grinding mill liner design and development.* Mining, Metallurgy & Exploration 24(3), 121–132.

SAFA, A., AISSAT, S., 2023. *Exploring the effects of a new lifter design and ball mill speed on grinding performance and particle behaviour: A comparative analysis.* Engineering and Technology Journal 41, 1–10.

SEBER, G.A.F., WILD, C.J., 2003. *Nonlinear Regression.* John Wiley & Sons, Hoboken, NJ.

SHI, F., et al., 2009. *Development of a rapid particle-breakage characterisation device: The JKRBT.* Minerals Engineering 22(7–8), 602–612.

SILVA, A.C., LUZ, J.A.M., 2012. *Continuous grinding mill simulation using Austin's model.* Exacta 10(3), 333–339.

SOLEYMANI, M. M., BAHIRAIE, M., & REZAEIZADEH, M., 2022. *Investigating the contribution of wear caused by impact and abrasion in semi autogenous grinding mills.* International Journal of ISSI, 19(2), 59-65.

TAVARES, L.M., KING, R.P., 1998. *Single-particle fracture under impact loading.* International Journal of Mineral Processing 54(1), 1–28.

TIBSHIRANI, R., 1996. *Regression shrinkage and selection via the Lasso.* Journal of the Royal Statistical Society: Series B 58(1), 267–288.

TINO, A.A., et al., 2023. *Measuring particle strengths and fracture-energy distributions with the Geopyörä.* Presented at Comminution '23, Cape Town, South Africa.

TOOR, P., PERKINS, T., POWELL, M., FRANKE, J., 2011. *The influence of liner wear on milling efficiency*. Presented at the Metallurgical Plant Design and Operating Strategies Conference, MetPlant 2011, Perth, Australia.

TROMANS, D., 2008. *Mineral comminution: Energy efficiency considerations.* Minerals Engineering 21, 613–620.

TUMBLING MILL (MEDIA TRAJECTORY), n.d. T*umbling mill: Media trajectory. Available at: https://wiki.metdynamics.com.au/view/Tumbling_Mill_(Media_Trajectory) (accessed 30 March 2025).*

VAN DER WESTHUIZEN, A.P., POWELL, M.S., 2006. *Milling curves as a tool for characterising SAG mill performance.* In: Proceedings of the SAG Conference.

VOGEL, L., PEUKERT, W., 2002. *Characterisation of grinding-relevant particle properties by inverting a population balance model.* Particle & Particle Systems Characterization 19(3), 149–157.

WANG, G., XIAO, Q., WANG, X., LI, Y., JIN, S., WANG, M., ... & LIU, R., 2025. *Research on Optimization of Lifter of an SAG Mill Based on DEM Simulation and Orthogonal Tests and Applications.* Minerals, 15(2), 193.

WANG, J., ZHOU, L., LIU, S., DENG, Z., CAO, Z., LI, P., 2025. *An advanced calibration technique for contact parameters in ball milling DEM simulations.* Powder Technology 454, 120716. https://doi.org/10.1016/j.powtec.2025.120716.

WANG, Y., et al., 2017. *Parameter identification for breakage distribution function of bauxite based on state transition algorithm.* In: Proceedings of the 6th International Symposium on Advanced Control of Industrial Processes, AdCONIP 2017. IEEE.

WEERASEKARA, N.S., et al., 2013. *The contribution of DEM to the science of comminution.* Powder Technology 248, 3–24.

WHITE, H., 1905. *The theory of the tube mill.* Journal of the Chemical, Metallurgical and Mining Society of South Africa, 290–305.

WILLS, B.A., FINCH, J.A., 2016. *Wills' Mineral Processing Technology: An Introduction to the Practical Aspects of Ore Treatment and Mineral Recovery, 8th ed. Elsevier.*

XU, L., LUO, K., ZHAO, Y., 2018. *Numerical prediction of wear in SAG mills based on DEM simulations.* Powder Technology 329, 353–363.

YAHYAEI, M., BANISI, S., & HADIZADEH, M., 2009. *Modification of SAG mill liner shape based on 3-D liner wear profile measurements.* International Journal of Mineral Processing, 91(3-4), 111-115.

YAHYAEI, M., BANISI, S., 2010. *Spreadsheet-based modeling of liner wear impact on charge motion in tumbling mills.* Minerals Engineering 23(15), 1213–1219.

YUAN, C., et al., 2023. *A new approach to the grinding kinetics of magnetite ore based on the population balance model.* Minerals 13(3), 424.

ZHANG, D., et al., 2024. *Semi-autogenous mill power-consumption prediction based on CACN-LSTM.* Applied Sciences 15(1), 2.

ZHAO, Y., et al., 2017. *An erosion model for the discrete element method.* Particuology 34, 81–88.

ZHU, Q., FENG, Y., WITT, P., BRUCKARD, W., & YANG, R., 2025. *Investigation of the effect of lifter configuration on wet grinding and wear in an industrial-scale SAG mill with GPU-powered CFD-DEM modelling.* Powder Technology, 458, 120959.